GNSS Positioning Aided with Pedestrian Dead Reckoning (PDR) in Urban Areas

Huan Luo, Duojie Weng, Ahmed Mansour, Xiaolong Mi, Yang Yang, Wu Chen

***Abstract*— Urban environments, characterized by dense high-rise buildings and narrow streets, present substantial challenges to GNSS positioning due to signal blockages and multipath effects. The conventional fault detection and exclusion (FDE) methods struggle in these settings because the majority of measurements contain multipath or non-line-of-sight (NLOS) errors. To address these challenges, a novel pedestrian dead reckoning (PDR)-aided FDE framework is proposed to enhance GNSS positioning accuracy in urban canyons. In this framework, the constraints are firstly derived from PDR and the receiver clock error, and these constraints are then used to enhance GNSS positioning through clustering. Both static and dynamic tests were carried out to evaluate the performance of the proposed system. Results show that the proposed approach achieves accuracies of 1.7m–11.5m, compared to 4.2m–57.4m for chip outputs, while the conventional FDE method is impractical in deep urban canyons since its availability extremely decreased to 3.2%. Kinematic tests in Hong Kong reveal a 52.4% enhancement in root mean square (RMS) accuracy (12.9m vs. 27.6m for chip outputs) with 100% availability. This work provides a computationally efficient, hardware-independent solution for reliable urban positioning on consumer devices.**

***Index Terms*—Fault detection and exclusion (FDE), urban positioning, smartphones, pedestrian dead reckoning (PDR)**

I. INTRODUCTION

POSITIONING is essential for various applications, such as location-based services (LBS), intelligent transport systems (ITS), navigation, emergency responses, and delivery services, significantly boosting convenience for individuals [1-3]. Among the platforms enabling these applications, smartphones are the most prevalent due to their widespread adoption, sensor capabilities, processing power and cost-effectiveness [4]. Equipped with affordable global navigation satellite system (GNSS) chipsets and antennas, smartphones have gained extensive attraction for accurate positioning. The release of Android 7.0 in 2016, which allowed users access to the raw GNSS measurements from Android-based smartphones, has further spurred interests in enhancing the GNSS performance mounted on those devices [5].

While GNSS technology in smartphones can achieve meter-level accuracy in open areas, urban environments present significant challenges [6]. In these environments, dense buildings often results in multipath interference and non-line-of-sight (NLOS) reception, which are commonly categorized as multipath effects [7]. These effects severely degrade the GNSS positioning performance, limiting its applications in urban regions [8]. With urban population expected to reach 68% by 2050, there is an urgent need to improve positioning accuracy in urban positioning on consumer-grade devices [9].

Various techniques have been developed to mitigate multipath effects in urban areas. The hardware approach uses the advanced antenna and receiver designs to mitigate multipath effects [10-13]. However, these technologies are often impractical for mass-market devices due to size and cost constraints. Receiver autonomous integrity monitoring (RAIM)-based and subset-based fault detection and exclusion (FDE) stands out as another approaches [14-19]. These methods can work without requiring external databases or specialized hardware, making it suitable for consumer-grade devices. By leveraging redundant satellite measurements and statistical consistency checks, FDE can enhance positioning performance in open-sky environments, where LOS signals dominate. However, their performance can be degraded significantly in urban canyon environments, where the majority of measurements are affected by large errors. As a result, FDE struggles to distinguish LOS and NLOS signals, leading to wrong or incomplete fault exclusion [9].

Some studies have used three-dimensional (3D) city models to mitigate multipath effects. Shadow matching is one typical approach through signal visibility prediction to improve GNSS urban positioning [20]. It can enhance positioning accuracy in the cross-street direction [21-26]. However, it is insensitive to localization in the along-street direction. Another 3D mapping-aided (3DMA) methods use range measurements [27-32]. Different from the prediction of signal visibility, these approaches exclude or correct NLOS signals with the aid of 3D models in the measurement domain. These methods can improve horizontal positioning performance in urban environments, outperforming shadow matching. However, the calculation of visibility and path delays is computationally intensive, rendering it infeasible for consumer-grade devices. More importantly, they depend on high-resolution 3D city

This work was supported in part by the Guangdong Basic and Applied Basic Research Foundation under Grant 2026A1515011534, Research Grants Council of Hong Kong through the Hong Kong General Research Fund under Grant 15229622 and the Guangdong - Hong Kong Technology Cooperation Funding Scheme under Grant GHP/033/22SZ. *(Corresponding author: Duojie Weng and Wu Chen).*

Huan Luo, Yang Yang, Xiaolong Mi and Wu Chen are with the Department of Land surveying and Geo-Informatics, The Hong Kong Polytechnic University, Hong Kong (e-mail: hilary.luo@connect.polyu.hk; e-mail: yyoung.yang@polyu.edu.hk;xiaolong.mi@polyu.edu.hk; wu.chen@polyu.edu.hk).

Duojie Weng is with the Ministry of Natural Resources (MNR) Key Laboratory for Geo-Environmental Monitoring of Great Bay Area & Guangdong Key Laboratory of Urban Informatics, Shenzhen University, Shenzhen, China (e-mail: djweng@szu.edu.cn).

Ahmed Mansour is with the Department of Land surveying and Geo-Informatics, The Hong Kong Polytechnic University, Hong Kong, and the Department of Public Works, Cairo University, Egypt (ahmed.m.mostafa@connect.polyu.hk).

models, which are not accessible in lots of areas [33, 34]. Therefore, it is crucial to develop an efficient FDE method without a 3D model for mass positioning-related applications on consumer-grade devices.

An alternative approach explores onboard sensors in consumer-grade receivers, such as accelerometers, gyroscopes, magnetometers, barometers, to assist GNSS technology [35-39]. Pedestrian dead reckoning (PDR) is a self-contained technology to provide precise relative movements without external data, and it has been widely used to enhance urban positioning [36, 40, 41]. Several studies have highlighted PDR's ability to achieve remarkable accuracy in short-term scenarios, effectively filling the gap of GNSS outages [42, 43]. Nevertheless, it is susceptible to drift errors, accumulating quadratically over time. In case that GNSS performance is continuously limited in urban environments, PDR proves ineffective in augmenting positioning accuracy [44]. Therefore, the key problem lies in providing accurate absolute positioning solutions at a relatively high frequency to calibrate its drift, further improving GNSS positioning performance.

In this study, a new algorithm is proposed through tight integration of GNSS observations and inertial measurement unit (IMU) data for urban positioning. The key contributions of this study are as follows:

(1) We propose an innovative approach for identifying fault-free measurements, assisted by PDR technology. Unlike conventional FDE methods that rely on inter-satellite consistency checks and fail when multiple faults are present, our approach adopts IMU data to remove pedestrian location changes from pseudorange measurements, enabling satellite-by-satellite fault detection independent of inter-satellite coupling. This fundamentally overcomes the limitation of conventional methods in dense urban canyons where most measurements are contaminated.

(2) We present a novel weighting method through residual clustering, where residual discrepancies between satellites serve as an indicator for the second-step FDE. This addresses the challenge of identifying faults with small variations (e.g., stable NLOS signals) that remain undetected after the first-stage FDE, thereby improving the purity of fault-free satellite selection.

(3) We introduce an enhanced positioning scheme, namely grid weight smoothing and clustering (GWSC), that addresses the lack of robustness in single-epoch solutions. By applying temporal smoothing to multi-epoch grid weights and spatial clustering in the position domain, GWSC effectively suppresses epoch-to-epoch fluctuations and strengthens consistent candidate regions, significantly improving positioning stability in challenging environments.

(4) Extensive experiments have been conducted in typical dense urban areas, covering a range of urban canyon densities and performing both static and kinematic tests. Unlike previous studies that often evaluate methods in a single environment, our comprehensive evaluation across low-, middle-, and high-density urban canyons demonstrates significant improvements in accuracy and reliability across diverse urban scenarios.

The structure of this paper is outlined as follows. Section II introduced the challenges encountered by conventional GNSS FDE methods. Section III presents an in-depth overview of the proposed method. In Section IV, the performance of the proposed algorithm is assessed by a comprehensive analysis with step-by-step illustrations and several experiments. Finally, the conclusion and discussion are demonstrated in Section V.

II. Challenges of conventional GNSS FDE

The primary observation used in low-cost GNSS receivers is pseudorange

$$\rho^i = \left\|\boldsymbol{x}^i - \boldsymbol{x}\right\| + b - b^i + I^i + T^i + \alpha^i m_\rho^i + \varepsilon_\rho^i \tag{1}$$

where ρ^i denotes the pseudorange of satellite i; $\boldsymbol{x}^i$ represents position of satellite i; $\boldsymbol{x}$ indicates the receiver position being estimated; b stands for the bias in the receiver clock, which is uniform across all satellites; b^i represents the clock error of the satellite i; I^i and T^i indicate the ionospheric delay and tropospheric delay for satellite i, respectively; α^i is a binary variable with taking the value 0 for satellites free from multipath effects and 1 for satellites affected by multipath; m_ρ^i denotes the pseudorange error due to the multipath and NLOS; ε_ρ^i is the measurement noise.

The linearized equation at the initial receiver's position $\boldsymbol{x_0}$ is given as

$$\Delta\boldsymbol{\rho} = \overline{\boldsymbol{\rho}} - (\|\boldsymbol{x} - \boldsymbol{x_0}\|) = \boldsymbol{H}\Delta\boldsymbol{x} + \boldsymbol{e} \tag{2}$$

where bold fonts represent matrix or vector; $\overline{\boldsymbol{\rho}}$ represents the corrected pseudorange observation vector; $\Delta\boldsymbol{x}$ indicates the unknown parameters of the 3-dimensional (3D) receiver position and receiver clock; $\boldsymbol{e}$ is the observation error term; $\boldsymbol{H}$ denotes the observation matrix, representing the relative geometry between the line-of-sight (LOS) vectors of satellites and the receiver.

When the dimension of observation vector is greater than that of unknow parameters, the unknowns can be estimated based on the weighted least squares

$$\Delta\hat{\boldsymbol{x}} = (\boldsymbol{H^T W H})^{-1}\boldsymbol{H^T W}\Delta\boldsymbol{\rho} = \boldsymbol{H}^*\Delta\boldsymbol{\rho} \tag{3}$$

where $\boldsymbol{W}$ denotes the weight matrix of observations, which are commonly determined by three schemes: C/N_0 -based weighting, elevation-based weighting, and equal weighting [7], $\boldsymbol{H}^*$ is defined as the pseudo inverse of observation matrix $\boldsymbol{H}$, expressed as $\boldsymbol{H}^* = (\boldsymbol{H^T W H})^{-1}\boldsymbol{H^T W}$.

The pseudorange residual vector can be expressed as

$$\boldsymbol{v} = \Delta\boldsymbol{\rho} - \boldsymbol{H}\Delta\hat{\boldsymbol{x}} = (\boldsymbol{I} - \boldsymbol{H}\boldsymbol{H}^*)\boldsymbol{e} = \boldsymbol{S}\boldsymbol{e} \tag{4}$$

and matrix $\boldsymbol{S}$ can be given by

$$\boldsymbol{S} = \boldsymbol{I} - \boldsymbol{H}\boldsymbol{H}^* \tag{5}$$

where matrix $\boldsymbol{I}$ is an identity matrix that has the same dimensions as the matrix HH^*.

As shown in (4), the residual $\boldsymbol{v}$ is the product of the observation errors and the matrix $\boldsymbol{S}$. Since $\boldsymbol{v}$ is a linear combination of $\boldsymbol{e}$, a large residual of a particular satellite i does not mean that the observation error of this satellite is large.

Faulty measurements can be detected and excluded through checking the consistency among residuals, and this method is called conventional FDE method [45]. However, this method struggles under the condition of multiple faults, especially in the cross-street direction where redundancy of fault-free observation is limited [20].

III. Methodology

PDR, as the key technology for providing accurate relative changes of the pedestrian, it can be potentially used as a baseline to mitigate the faulty measurements within a period of time. In this section, PDR is integrated with GNSS to mitigate GNSS outliers due to multipath and NLOS errors.

As illustrated in Fig. 1, the framework of the proposed method employs a two-stage algorithm - PDR-aided FDE algorithm and positioning scheme - to achieve accurate positioning. First, IMU data and pseudorange measurements are tightly integrated for FDE with receiver clock constraints. In this stage, the motion-induced variations are derived from PDR, and they are removed from GNSS equations, and in this way, fault can be detected satellite by satellite. Second, residuals generated across all grids are evaluated, where time-series residuals from fault-free satellites are spatially clustered to score grid likelihoods. This method involves the second-step FDE across various grid points through clustering satellites with small residual discrepancies. Finally, the filtering method dynamically smooths and clusters grid weights based on IMU-predicted motion and residual-driven scores.

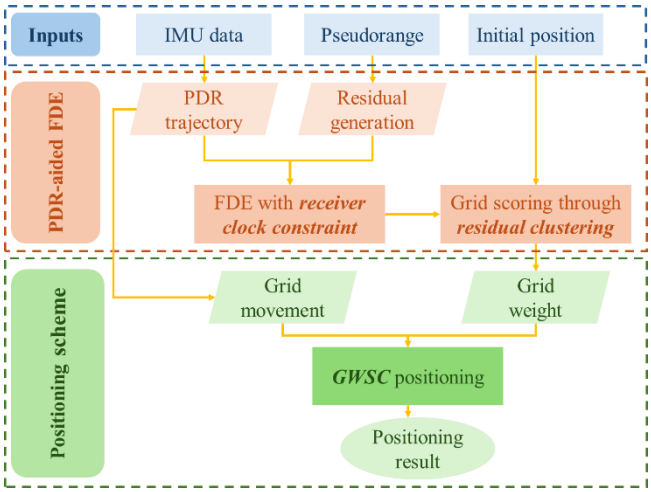

Fig. 1. Framework of the proposed method.

A. PDR

PDR is a relative positioning technique that estimates a person's new position by adding their estimated step length and direction (heading) to a previously known location, using data from sensors such as accelerometers, gyroscopes, and magnetometers. Unlike absolute positioning methods like GPS, PDR does not rely on external infrastructure, but its accuracy degrades over time due to the accumulation of sensor errors. This study employs the short-term PDR relative trajectory to constrain corresponding GNSS positions, thereby reducing the number of position unknowns in observation equations to three during this period.

Suppose that the starting position $\boldsymbol{p}_{dr}(1)$ has an error $\Delta\boldsymbol{x}$ in position, where $\Delta\boldsymbol{x} = \boldsymbol{x}(1) - \boldsymbol{p}_{dr}(1)$. The relative errors in PDR positions are negligible over short time intervals. Under this assumption, we can deduce the following equation

$$\Delta\boldsymbol{x} = \boldsymbol{x}(k) - \boldsymbol{p}_{dr}(k) \tag{6}$$

where $\Delta\boldsymbol{x}$ represents the unknown parameter to be estimated; k denotes the time index, $\mathrm{k} = 1,2,\ldots m$, and m stands for the window size.

Fig. 2 illustrates the relationship between $\boldsymbol{x}(k)$ and $\boldsymbol{p}_{dr}(k)$. The PDR positions $p_{dr}(k)$ are denoted as hollow circles, while the true positions $\boldsymbol{x}(k)$ are depicted as black circles over a short time span. As shown, there is a shift $\Delta\boldsymbol{x}$ between $\boldsymbol{x}(k)$ and $\boldsymbol{p}_{dr}(k)$ within the m epochs. In this study, the shift will be estimated with GNSS measurements that are free of multipath effects.

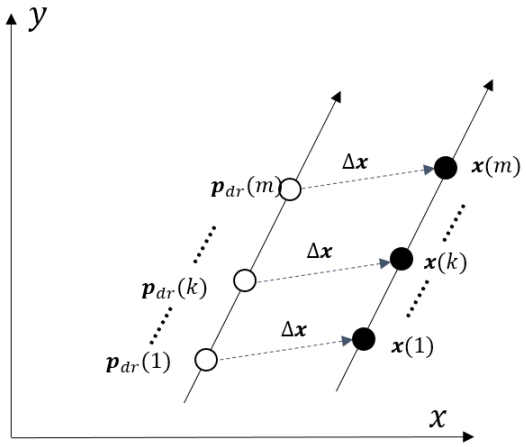

Fig. 2. Positioning sequence with biased position from PDR in a short time interval.

B. Multipath mitigation using constraints of PDR and the receiver clock error

Referring to (1), (2) and (6), the pseudorange measurement $\rho^i(k)$ is initially linearized around the corresponding PDR position $\boldsymbol{p}_{dr}(k)$, and the residuals can be given as

$$\begin{aligned} r^i(k) &= \rho^i(k) - \left\|\boldsymbol{x}^i(k) - \boldsymbol{p}_{dr}(k)\right\| - I^i(k) - T^i(k) + b^i(k) \\ &= \boldsymbol{a}^i(k)\Delta\boldsymbol{x} + b(k) + \alpha^i(k)m_\rho^i(k) + \varepsilon^i(k) \end{aligned} \tag{7}$$

where $r^i(k)$ is the measurement residuals at the position $\boldsymbol{p}_{dr}(k)$; $I^i(k)$ and $T^i(k)$ denote the ionospheric delay and tropospheric delay, respectively, and $b^i(k)$ presents the satellite clock error, which are mitigated via models or differential corrections; $\boldsymbol{a}^i(k)$ is LOS unit vector pointing from the satellite to the receiver; $b(t)$ is the bias in receiver clock that is common to all satellites tracked; α^i is a binary variable with 0 for multipath-free satellites, and 1 for satellites with multipath effects.

As discussed, the unknown position offset $\Delta\boldsymbol{x}$ in (7) can be assumed to remain constant during the short time, the LOS unit vector $\boldsymbol{a}^i(k)$ varies with the movement of the satellite. The distance between the satellites and the receiver is far larger than the distance changes of receiver or satellite, so the

changes in $\boldsymbol{a}^i(k)\Delta x$ should be small, which are evaluated with a GNSS receiver located in the open area as follows.

Assuming a positioning error $\Delta\boldsymbol{x}$ of 50 m, we have calculated the variations caused by the position bias for all satellites in a period of 60 seconds, denoted as $\boldsymbol{a}^i(k)\Delta\boldsymbol{x} - \boldsymbol{a}^i(1)\Delta\boldsymbol{x}$. Fig. 3 illustrates the changes for all received satellites in $\boldsymbol{a}^i(k)\Delta\boldsymbol{x} - \boldsymbol{a}^i(1)\Delta\boldsymbol{x}$ over this time span. The distinctively colored curves represent the variations for various satellites, illustrating each variation influenced by its respective orbital movements. The largest observed variation is less than 0.4 m over 60 seconds and less than 0.2 m within 30 seconds. Notably, these variations are significantly smaller than the impacts of multipath effects on pseudoranges. Therefore, $\boldsymbol{a}^i(k)\Delta\boldsymbol{x}$ is considered to be equal to $\boldsymbol{a}^i(1)\Delta\boldsymbol{x}$, hence, $\boldsymbol{H}(k) = \boldsymbol{H}(1)$, meaning that the observation matrix $\boldsymbol{H}$ remains the same during a short period.

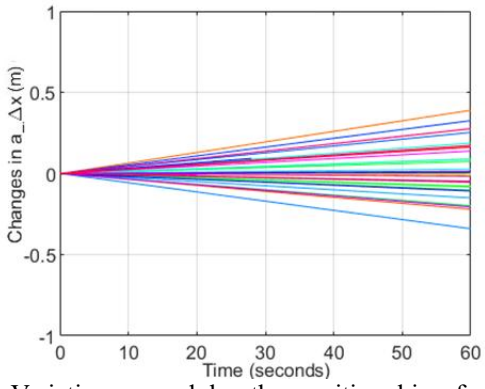

Fig. 3. Variation caused by the position bias for different satellites within a short period.

In (7), the error of the receiver clock $b(k)$ is common for all satellites, and it changes from epoch to epoch. Although previous research has indicated that the clock biases of low-cost receivers can be unpredictable and unstable over a long time [48], such as 12 hours, the receiver clock error can be modelled with a linear polynomial within a certain period (e.g. several seconds to minutes) [49], expressed as

$$c^*, d^* = \arg\max_{c,d} r^i(c,d) \tag{8}$$

$$b^*(k) = c^*k + d^* - \boldsymbol{a}^i(k)\Delta\boldsymbol{x} \tag{9}$$

where c^* and d^* denotes the slope and intercept of linear regression of r^i from LOS signals, respectively.

Fig. 4 illustrates an example of pseudorange residual errors corresponding to (7) during a short period. It comprises three parts: the first error term $\boldsymbol{a}^i(k)\Delta\boldsymbol{x}$ caused by biased position sequences, the receiver clock error term $b(k)$, and the multipath-induced error term $\alpha^i(k)m_\rho^i(k)$. The first and the second term can be constant and modeled during a short period, respectively, as discussed, while the third term varies depending on environmental changes. When measurements contain multipath errors, $\alpha \neq 0$, the variation of pseudorange will increase [50]. By analyzing the residual variability after detrending, measurements contaminated by multipath effects can be identified: if a satellite's detrended residual shows significant fluctuations, it will be regarded as a fault; otherwise, it might be fault-free. Therefore, the variation of the time-series residuals is introduced as an important indicator for fault identification.

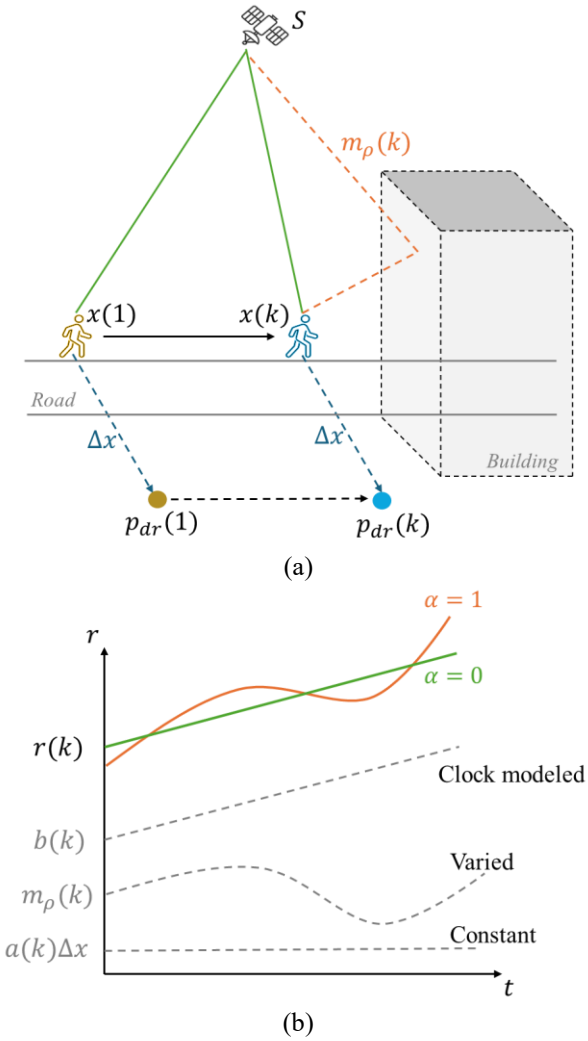

Fig. 4. (a) Example of observation errors during walking in urban areas; (b) Illustration of errors in measurement residuals during a short period.

For the time-series residuals r, we can introduce a receiver clock constraint to detect and exclude the satellites that are affected by the multipath effects ($\alpha^i \neq 0$). If the satellites are contaminated, their time-series residuals will experience fluctuation and/or be discontinuous due to changes in the environment or reflection points. Therefore, the time-series residuals can aid in identifying signals contaminated by multipath effects.

The trend of the time-series residuals from all satellites can be modeled and removed based on linear regression on residuals referring to (9). Then, the continuity and the variation of the detrended time-series residuals in the period, $det(r^i) = r^i - b^*$, is innovatively monitored to detect the multipath effects, expressed as

$$S^i(m) = \underset{k=1:m}{STD}\ det(r^i) \tag{10}$$

$$P^i(m) = \frac{SC_i}{m} \tag{11}$$

where $P^i(m)$ is the continuity indicator of satellite i in the previous m epochs; SC_i denotes epoch counts of measurements from satellite i; $S^i(m)$ is the moving standard deviation; STD is the operation for moving standard deviation.

C. Grid scoring through residual clustering

The FED presented in the previous subsection effectively identifies those faults with large variation or discontinuity, however, some faults with small variation remained, e.g. NLOS signals with stable reflection surface. To identify remaining faults, the discrepancies of detrended residuals between remaining satellites were employed to exclude satellites on each grid. And then, the satellite quality and detrended residuals' discrepancies of the clustered group were applied as the indicator to score each grid.

Referring to (9), for LOS signals ($\alpha^i = 0$), if the PDR positions have no errors ($\Delta \boldsymbol{x} = 0$), the detrended time-series residuals $det(r^i)$ would be same for different satellites during a short period; If there is a bias in PDR trajectory ($\Delta \boldsymbol{x} \neq 0$), the detrended residuals from LOS signals should have discrepancies, since $\boldsymbol{a}^i$ relates to the geometry over the satellite $\boldsymbol{S}^i$ and the receiver, hence, if the azimuths and/or elevation of satellite i and j are different, we can infer that $\boldsymbol{a}^i(k)\Delta \boldsymbol{x} \neq \boldsymbol{a}^j(k)\Delta \boldsymbol{x}$.

To cluster the remaining satellites, a reference satellite is selected based on the satellite quality, deriving from weights of the variation ($W_S = \frac{1}{S^i(m)}$) and the continuity ($W_P = P^i(m)$) of the detrended time-series residuals.

Given the varying units and interpretations of the parameters mentioned, they are initially normalized. The combined normalized weights indicate the satellite quality, as shown by:

$$W_{q_{S_i}} = \sum_{j=1}^{2} W_j' \tag{12}$$

where W_j' represent the normalized weights for residuals variation and residuals proportion of satellite S_i, respectively.

The satellite with the highest weight, referring to (12), is then selected as the clustering reference satellite ($S_{ref} = \arg\max_{S_i} W_q$). The discrepancies of the detrended residuals related to the reference satellite can be expressed as

$$\Delta det(r^{S_i}) = det\left(r^{S_{ref}}\right) - det(r^{S_i}) \tag{13}$$

where $det\left(r^{S_{ref}}\right)$ and $det(r^{S_i})$ represent the detrended residuals from the reference satellite and i^{th} satellite, respectively; $\Delta det(r^{S_i})$ indicates the discrepancies of the detrended residuals between the reference satellite and the i^{th} satellite.

The clustered group is then formed by considering satellites whose residual differences meet a specific threshold criterion, $\Delta det(r)^T$.

$$S_i \in G_{S_{ref}}, \qquad (\Delta det(r^{S_i}) \leq \Delta det(r)^T) \tag{14}$$

where $G_{S_{ref}}$ denotes the determined satellite group. When the PDR positions have no errors, the discrepancies over LOS signals will vary within the measurement noise. Therefore, the threshold, $\Delta det(r)^T$, for the group satellites can be set based on the level of measurement noises of receiver.

The outliers are excluded on each grid based on the clustering approach. Instead of employing the least squares method for position determination, a likelihood-based approach is employed, where grid scores are calculated based on the quality of the clustered satellite group and the detrended residuals' discrepancies of the satellite group. The first term can be derived referring to (12) and the weight derived from the discrepancies is defined as the reciprocal of detrended residuals' discrepancies ($W_{I_{S_i}} = \frac{1}{\Delta det(r^{S_i})}$).

The grid scores can be expressed as

$$W_g = \sum_{S_i} \left(W_{q_{S_i}}{}' + W_{I_{S_i}}{}'\right), \quad \left(S_i \in G_{S_{ref}}\right) \tag{15}$$

where $W_{q_{S_i}}{}'$ and $W_{I_{S_i}}{}'$ are the re-normalized weight of satellite quality and detrended residuals' discrepancies corresponding to the satellite S_i, respectively. A larger weight of the candidate indicates that the candidate point is closer to the true location, and the positioning solution is obtained based on the grid weight.

D. Positioning scheme

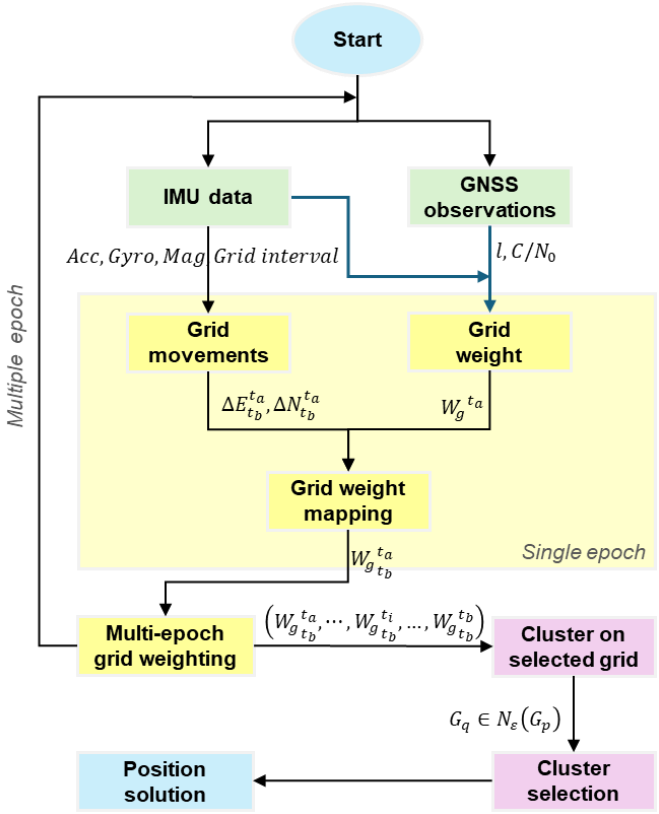

Fig. 5. Illustration of GWSC positioning scheme.

This study applies a robust positioning scheme incorporating dynamic error smoothing and clustering, namely GWSC, which is adopted from our previous research [32], to obtain the optimal candidates based on the time-series pseudorange residuals, as illustrated in Fig. 5. The algorithm contains a two-stage positioning approach: dynamic weight smoothing (the yellow part) and clustering approach (the pink part).

The horizontal distance change of receiver between two epochs (t_a, t_b) can be calculated based on IMU sensor data. By dividing the grid interval, the receiver's movements can be approximated as the grid movements from t_a to t_b, resulting in $\Delta E_{t_b}^{t_a}$ and $\Delta N_{t_b}^{t_a}$, representing movements in the easting and northing direction, respectively. Concurrently, the grid weights at epoch t_a, denoted as ${W_g}^{t_a}$, can be derived referring to (15). Combining the grid movements, the weight of grid ${W_g}^{t_a}$ can be mapped from epoch t_a to epoch t_b.

Through iterative mapping of grid weights, a sequence of weights associated with a specific grid g can be mapped from historical data to the current epoch, denoted as $\left(W_{g_{t_b}}^{t_a}, \cdots, W_{g_{t_b}}^{t_i}, \ldots, W_{g_{t_b}}^{t_b}\right)$. Over a short duration, the current grid weight can be filtered through averaging in the sliding window, expressed as

$$\overline{W_{g_{t_b}}} = \frac{1}{b}\sum_{i=a}^{b} W_{g_{t_b}}^{t_i} \tag{16}$$

Based on the smoothed weights of all current candidates, a clustering approach is conducted to classify the qualified candidates with high weights into groups corresponding to locations. Density-based spatial clustering of applications with noise (DBSCAN) algorithm is a classic clustering algorithm that identifies clusters of varying shapes and sizes in a dataset based on the density of data points in the feature space, such as position domain [51]. The selected candidates, whose filtered grid weights are the largest, are determined. Next, these selected candidates are clustered into groups, expressed as

$$G_q \in N_\varepsilon(G_p), N_\varepsilon(G_p) \geq MinPts \left(G_q, G_p \in G^{selectd}\right) \tag{17}$$

where G_q and G_p are points in the group of selected candidate $G^{selectd}$, ε specifies the radius of the circle area as the eps-neighbor, $N_\varepsilon(G_p)$ is the set of points within the ε neighborhood of G_p, and $MinPts$ sets the requirement of the minimum number of points to form a cluster.

The counts of candidates and their corresponding weights within each group serve as the basis for identifying the ultimate group, afterwards, the ultimate group is used to establish the positioning solution as follows

$$X(E,N)^{t_j} = \frac{1}{\sum_p \overline{W}} \sum_p \overline{W} \cdot G_p(E,N), \left(G_p \in G_{DBSCAN}^u\right) \tag{18}$$

where G_p is the p_{th} grid included in the ultimate DBSCAN group (G_{DBSCAN}^u), $\overline{W}$ indicates the filtered grid weight in epoch t_j, and E and N indicate the easting and northing coordinate, respectively.

IV. Experiment Results

A. Experiment setup

To assess the performance of the proposed system, comprehensive experiments were conducted in Hong Kong, a city known for its challenging urban environments. These experiments included both static and kinematic tests, encompassing a range of urban canyon densities from low to high, as shown in Fig. 6. We utilized a consumer-grade Huawei P40 smartphone, equipped with IMU sensors and GNSS chips, to collect diverse data types, including accelerometer, gyroscope, magnetometer, barometer readings, as well as GNSS measurements comprising L1 pseudorange, carrier phase, Doppler, and C/N_0 values. The data acquisition frequencies were configured to 50Hz for IMU data and 1Hz for GNSS data.

All experiments were conducted in two distinct urban locations, Mong Kok (MK) and Wan Chai (WC), characterized by narrow streets and towering buildings. These two regions represent the typical urban canyons, with MK being moderately urbanized and WC being deeply urbanized. We performed nine static experiments, each lasting 4-5 minutes, and a kinematic test covering approximately 2270 meters in WC. The main streets generally align in approximate north-south and east-west directions. Based on visibility boundaries, related to street widths, building heights and sheltered spaces, all static experiments can be categorized into three types of densities: low- (green marker), middle- (red marker), and high- (yellow marker) density of urban environments, as shown in Fig. 6.

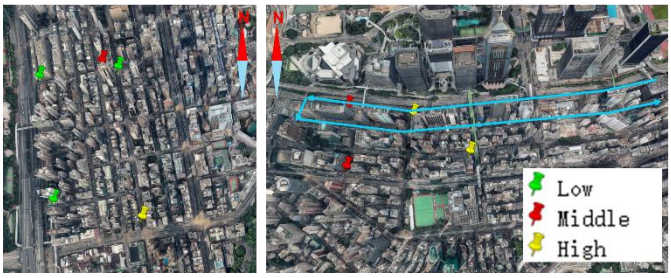

(a) (b)

Fig. 6. Environments of the testing areas.

The accurate coordinates of all lampposts are provided by the Hong Kong Lands Department. In static experiments pedestrians held the phones beside the lampposts, and the ground truths were extracted from the reference lampposts. In kinematic tests, lamppost IDs were recorded as pedestrians passed lampposts, with ground truth points generated by interpolation, achieving an error ratio of less than 1% from our prior research on PDR techniques [36, 52].

B. Characteristics demonstration of PDR-FDE algorithm

To thoroughly assess the principles and evaluate the efficiency of the innovative algorithm, a comprehensive analysis was first conducted, including PDR-FDE framework and positioning scheme using time-series measurements with field experimental data.

An example, collected in deep urban canyons, is illustrated in Fig. 7 and Fig. 8 to validate the two-step FDE method. Upon detrending the receiver clock error during a short period, time-series detrended residuals with the input of ground truth $(\Delta \boldsymbol{x} = 0)$ is shown in Fig. 7, while Fig. 8 illustrates the utilization of the sky mask, a product of our previous research efforts [32], to elucidate the performance of fault identification based on the proposed FDE method. Anomalies characterized by significant fluctuations (colored in yellow) are recognized as faults and excluded during the first FDE phase. Leveraging PDR technology, these faults were identified and excluded independently satellite-by-satellite. After the first FDE step,

residual faults persist (depicted in blue). Subsequently, a second FDE step is executed on each grid. Fig. 7 displays fault measurements (colored in blue) distinct from fault-free measurements (colored in green). With residual clustering method, the remaining faults were excluded in this step, where signals contaminated by multipath effects were excluded. This example demonstrates that proposed method is effective in identifying multiple faults among all satellites.

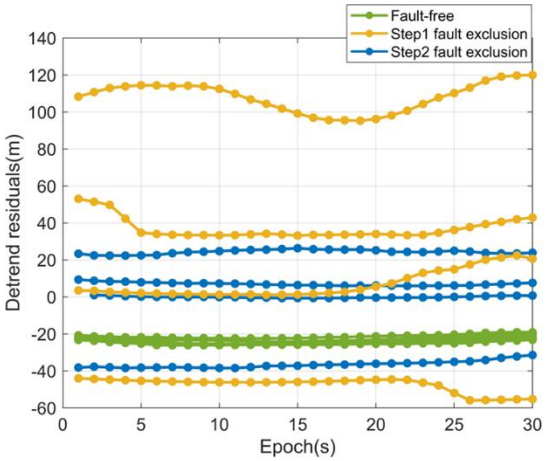

Fig. 7. An example of time-series residuals from different satellites on ground truth.

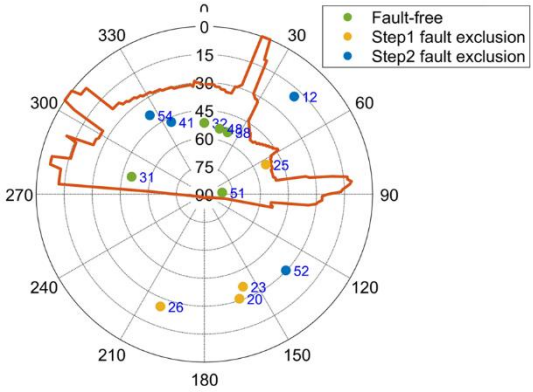

Fig. 8. Two-step fault detection based on time-series residuals.

To obtain the positioning solutions, the second FDE approach was conducted on all grid, and the grid weights of all candidates were calculated based on the residual discrepancy. The results of single epoch were used to illustrate the weight distribution, as shown in Fig. 9 (a). Grids centered on the figure had higher weights than those on the sides. However, these high weights are similar, and the positioning error of this epoch from the proposed method is relatively large, around 14m. By adopting the proposed smoothing scheme, GWSC method, the weight of the grid points close to the true value is strengthened, as shown in Fig. 9 (b).

To better understand the source of improvement, we analyzed intermediate outputs as illustrated in Fig. 9. Applying only the PDR-aided FDE stage (without GWSC smoothing) reduced the mean positioning error from 41 m (chip output) to approximately 14 m. Adding the full GWSC scheme further reduced the error to 3 m. This suggests that roughly 71% of the total improvement stems from better satellite/measurement selection via the two-stage FDE, while the remaining 29% is attributable to the temporal smoothing and clustering effects of GWSC, which suppress short-term fluctuations and reinforce consistent candidate regions.

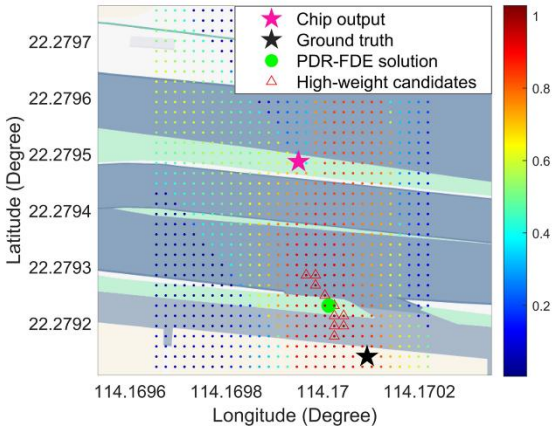

(a)

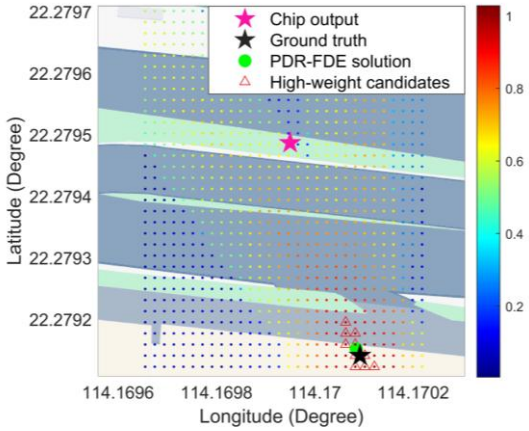

(b)

Fig. 9. Illustration of grid weight distribution from the proposed PDR-FDE method: (a) single epoch solution and (b) multi-epoch solution.

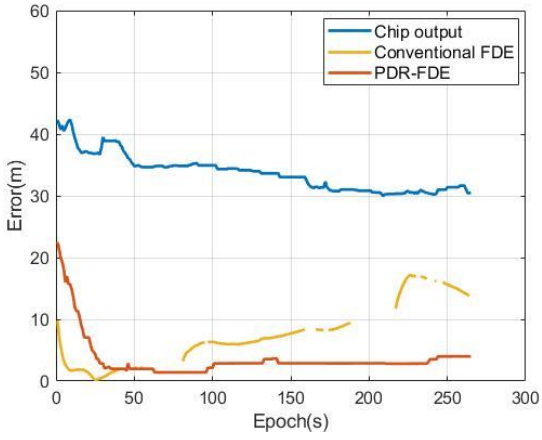

Fig. 10. Comparison of positioning errors from different strategies.

TABLE I
COMPARISON OF POSITIONING ACCURACY BETWEEN RAW GNSS OUTPUTS AND THE PROPOSED PDR-FDE METHOD IN URBAN CANYONS

Urban density	Test ID	Accuracy (m)			Availability (%)	
		Chip output	Conventional FDE	PDR-FDE	Conventional FDE	PDR-FDE
Low	**1**	8.8	7.1	**2.0**	100.0%	**100.0%**
	2	4.2	2.7	**1.7**	99.1%	**100.0%**
	3	10.1	2.7	**1.6**	94.8%	**100.0%**
Middle	**4**	13.2	8.7	**6.9**	33.8%	**100.0%**
	5	33.9	9.0	**7.0**	70.4%	**100.0%**
	6	31.5	10.4	**3.7**	88.5%	**100.0%**
High	**7**	16.8	22.9	**4.9**	66.5%	**100.0%**
	8	57.4	88.1	**8.5**	6.5%	**100.0%**
	9	37.9	24.2	**11.5**	3.2%	**97.5%**

The positioning solutions of all epochs from three strategies, including chip outputs (NMEA, i.e., National Marine Electronics Association standard sentences output by the GNSS chipset), conventional FDE, and PDR-FDE approach, were compared with ground truth, and their errors were plotted in Fig. 10. It indicates that the positioning errors of chip outputs ranged from 30m to 40m. Conventional FDE results were unstable and discontinuous, with errors from 1m to 17m. Our proposed method experienced initial convergence due to the GWSC algorithm, reducing positioning errors from 21m to 2m. The proposed method outperformed chip output, while the conventional method yielded discontinuous solutions with higher errors.

C. Pedestrian tests in static scenarios

The positioning accuracy of all static tests from chip outputs (NMEA results), conventional FDE method, and the proposed method are summarized in Table I, corresponding to the availability of two FDE methods. In all experiments, the root mean squares (RMS) of NMEA ranged from 4.2m to 57.4m. The conventional FDE method demonstrated improved accuracy in low- and middle-density urban environments. However, its availability decreased to 33.8%-88.5% in middle-density of urban regions. In highly urbanized areas, its errors exceeded those of the NMEA results, with availability decreasing to a range of 3.2% to 66.5%. In contrast, our proposed method exhibited significant enhancements in accuracy across various urban densities, achieving accuracy between 1.7m and 11.5m. Notably, in test 8, the positioning accuracy improved substantially from 57.4m to 8.5m. Although test 9 exhibited an availability of 97.5%, the remaining tests achieved a 100% availability rate. Consequently, the conventional FDE method proved ineffective in middle- and high- dense urban areas, while our proposed method delivered the highest positioning accuracy across diverse urban scenarios.

For a thorough evaluation of the performance of the three methods across varied urban scenarios, comparisons were carried out involving the cumulative distribution of horizontal positioning errors, RMS values, availability metrics, and improvement rates (IRs). Fig. 11 shows the cumulative distribution of horizontal positioning errors from different strategies conducted within three urban density scenarios. Meanwhile, Fig. 12 illustrates the positioning accuracy, availability and improvement rates among the three methods in diverse urban environments.

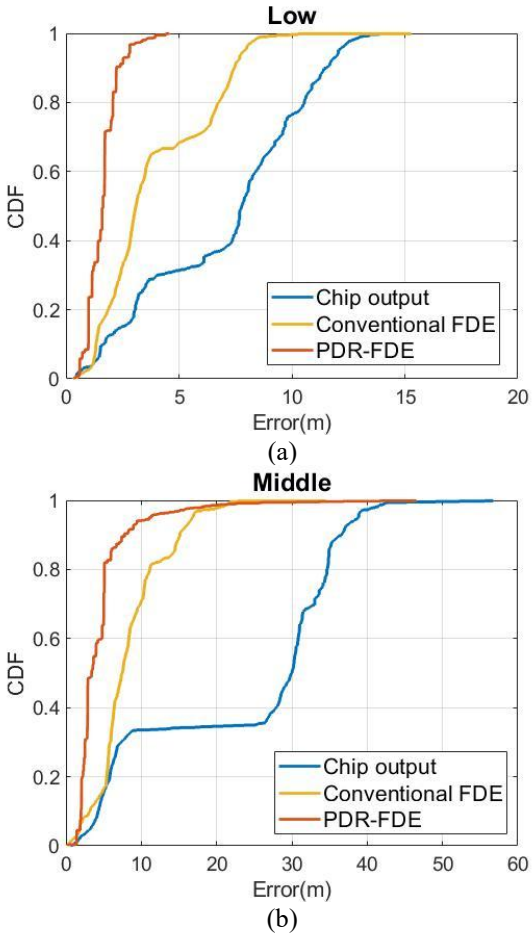

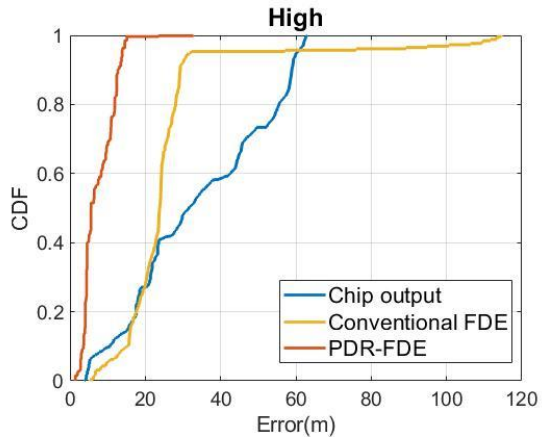

(c)

Fig. 11. Cumulative distribution of positioning errors from different strategies in static experiments under different densities of urban.

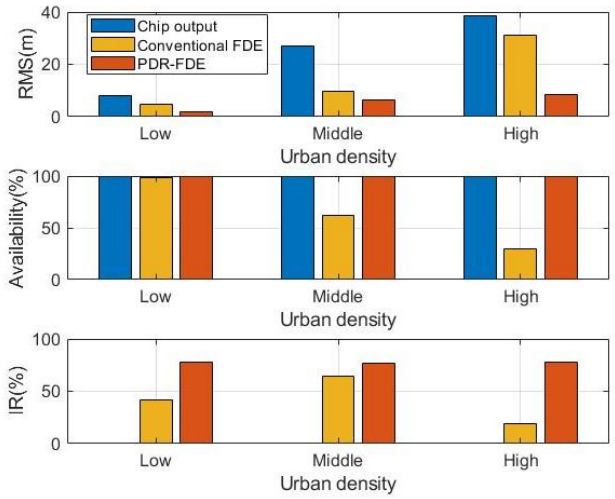

Fig. 12. Comparison of positioning accuracy, availability and improvement rates of RMS between three strategies under different density of urban areas.

In Fig. 11, it is evident that the CDF curves generated from chip outputs exhibited broad spreads and flat shapes across all urban area densities. Comparatively, the CDF curves derived from conventional methods displayed steeper shapes than those from chip outputs, but broader spreads. In contrast, the CDF curves produced by our proposed method demonstrated the narrowest spreads and the steepest shapes among the three methods across various urban scenarios. As a result, the proposed method yielded the highest percentage of solutions, falling within a smaller error range, and the accuracies of solutions from our method were the most consistent.

Fig. 12 provides an intuitive illustration of the RMS, availability and IRs among the three methods. In all densities of urban regions, the RMS values of chip outputs were the largest, while our proposed method consistently exhibited the smallest RMS values, ranging from 1.8m to 8.5m in three dense urban areas. Additionally, our method achieved an impressive improvement rate of approximately 77% over chip outputs in all urban densities. Although the conventional consistency check method demonstrated smaller RMS values than chip outputs, its availability significantly decreased with rising urban density. This indicates that although the conventional method can enhance positioning accuracy, its limited availability and reliability make it unavailable for moderate- to high-density urban environments. In summary, the conventional consistency check method can enhance accuracy but falls short in availability and reliability in denser urban landscapes. Conversely, our proposed method proves effective in achieving high positioning accuracy across diverse urban settings with excellent availability. Meanwhile, it emerges as the most reliable and robust approach among the three methods, particularly excelling in urban canyons.

D. Pedestrian tests in kinematic scenarios

To further evaluate the positioning performance of the proposed method, a kinematic experiment was carried out in complex environments, containing middle- and high-dense urban canyons. The conventional consistency check method has been proved unavailable in such complex environments. Therefore, a comparative analysis was performed solely between the data derived from the chip outputs and the results solved by the proposed method. Due to the availability of IMU data, an extended Kalman filter (EKF), adopted from our previous research [36], was integrated with the proposed method to smooth the solutions and improve the availability rate, considering that the availability rate might fall short of 100% during the kinematic assessment.

The chip outputs, depicted as blue points in Fig. 13, exhibited an average positioning accuracy of 27.6 meters. Notably, in high-dense urbanized regions, the positioning errors of the chip outputs deteriorated significantly, reaching up to 90 meters, as highlighted by the '1' red rectangle region in Fig. 13. In mediately dense urban areas, the positioning errors were between 30m and 40m, such as the '2' red rectangle region in Fig. 13. In such regions, pedestrians would be located on incorrect streets. By applying the proposed method (orange dots) and the EKF filtering method (green dots), the positioning solutions are shown in Fig. 13. Fig. 14 (a) demonstrates the cumulative distribution of horizontal positioning errors from three strategies, and comparison of RMS, availability rate and improvement rate are shown in Fig. 14 (b), and Table II depicts the performance of three strategies.

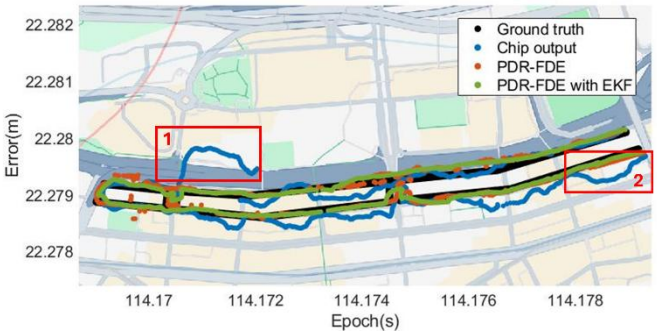

Fig. 13. Comparison of positioning results from different strategies in the kinematic experiment.

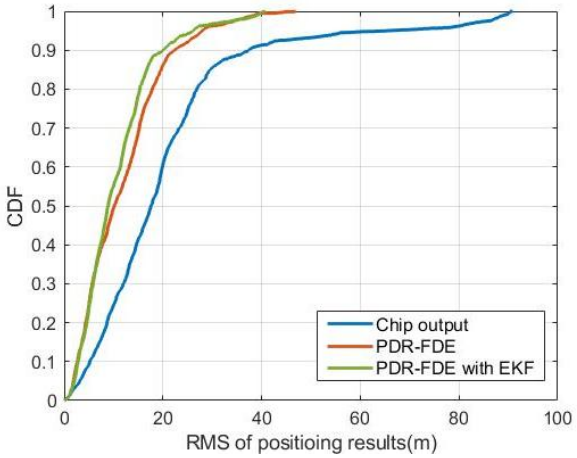

(a)

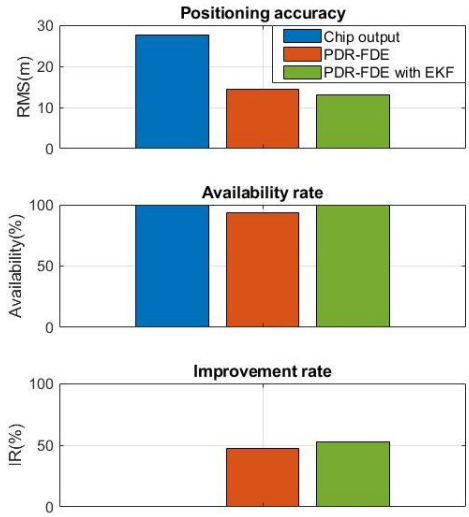

(b)

Fig. 14. (a) Cumulative distribution of positioning errors, and (b) the comparison of RMS, availability rate, and improvement rate from different strategies in kinematic experiments.

TABLE II
PERFORMANCE OF DIFFERENT STRATEGIES IN KINEMATIC EXPERIMENTS.

	Chip output	PDR-FDE	PDR-FDE with EKF
Mean error (m)	21.1	11.8	10.7
Maximum error (m)	90.8	46.9	40.8
Proportion (error<3m)	4.6%	11.3%	11.2%
Proportion (error <10m)	24.5%	46.1%	55.1%
Proportion (error >20m)	39.2%	12.9%	10.0%

By applying the proposed method, a significant proportion of solutions were located on the correct street, depicted as orange dots in Fig. 13. However, there were some outliers. Through the integration of inertial sensors using EKF, the filtered results exhibited enhanced continuity and smoothness, illustrated as green dots in Fig. 13. In Fig. 14 (a), the CDF curve of chip outputs was broader than that of IMU-aided methods, indicating larger errors associated with the chip outputs. Moreover, 50% and 90% of the results generated by chip outputs were approximately 18m and 37m, respectively, which were halved when applying the IMU-aided method. Summarized in Fig. 14 (b), the overall accuracy of the chip outputs stood at 28m. By employing the proposed method, this accuracy significantly improved to 14.4m, representing a 48% enhancement, but with an availability rate of 93.3%. After implementing the EKF method, the accuracy further improved to 12.9m, reflecting a 52.4% enhancement, with an availability rate reaching 100%.

As shown in Table II, the chip outputs showed a mean error of 21.1 m, which is reduced to 11.8 m using PDR-FDE and further refined to 10.7 m with EKF augmentation. Maximum errors are halved from 90.8 m (chip outputs) to 40.8 m (PDR-FDE with EKF), underscoring enhanced robustness against outliers. While high-precision outcomes (<3 m) remain limited (~11% for both FDE methods vs. 4.6% for chip outputs), moderate-accuracy reliability improves significantly, with 55.1% of errors below 10 m (PDR-FDE with EKF) compared to 24.5% from chip outputs. Notably, the proportion of large errors (>20 m) drops from 39.2% to 10%, highlighting the effectiveness of the proposed FDE method in mitigating severe failures.

A critical concern with any method that achieves high availability is whether it occasionally produces large undetected biases. Examining the tail of the error distribution addresses this question. As shown in Table II, the proportion of large errors (>20 m) is reduced from 39.2% (chip output) to just 10.0% (PDR-FDE with EKF), and the maximum error is more than halved (from 90.8 m to 40.8 m). These results confirm that the increased availability is accompanied by a substantial reduction in the frequency and magnitude of large outliers, demonstrating the method's integrity even in the most challenging urban segments.

For completeness, we evaluated PDR-only positioning performance in the kinematic test. As shown in Fig. 15, PDR achieved high relative accuracy over short distances but suffered from large drift over longer trajectories due to accumulated heading and step-length errors. In this test, unlike GNSS-based methods, PDR errors reached more than 100 m by the end of the trajectory. However, during a short period (e.g., 30 s windows), the positioning errors were within 5 m and 2 m for two representative segments (Period 1 and Period 2). In static tests, because the pedestrian is stationary, PDR step detection outputs zero displacement; thus the PDR position remains constant, and the error is simply the initial offset.

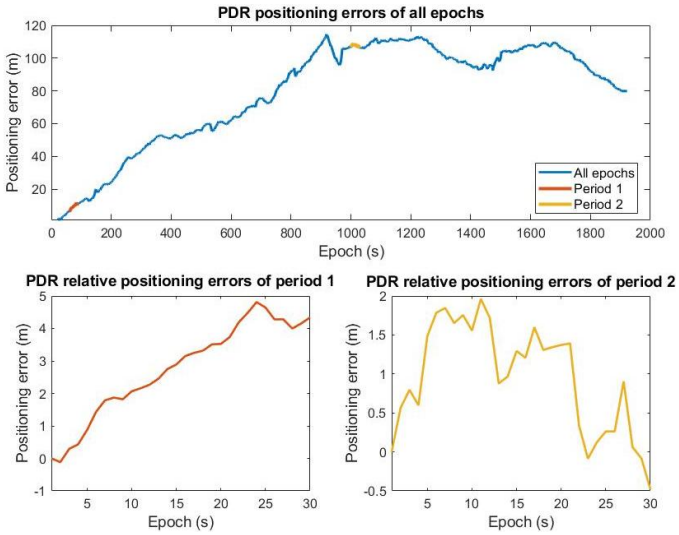

Fig. 15. Time series of horizontal positioning errors for PDR-only results in the kinematic test.

As shown in Fig. 15, the blue line shows the full trajectory error, reaching >100 m due to drift. The orange (Period 1) and yellow (Period 2) lines represent two 30-s windows extracted to illustrate relatively large and small PDR errors, respectively, demonstrating that PDR maintains sub-5 m accuracy over short intervals.

V. Conclusion and Discussion

This study presents a novel method for enhancing positioning accuracy in urban canyons through the integration of GNSS and IMU data. The approach leverages PDR-aided FDE on time-series measurements and a multi-epoch smoothing positioning scheme to address the challenges posed by dense urban environments.

The innovative algorithm was validated through comprehensive analysis for the two stages with filed data first. The FDE algorithm effectively identify fault measurements, showcasing that contaminated satellites were excluded through the two-step FDE approach. The subsequent stage involved calculating time-series pseudorange residuals between satellites to assess the grid weights. The experimental data showed that the novel weighting method identified the grids with high weight close to the ground truth. The proposed GWSC positioning scheme presented the ability to strengthen the grid weights around the true point. It significantly improved positioning accuracy from 41m to 3m, outperforming chip outputs (NMEA results) and traditional FDE methods.

In addition, the study compared the positioning accuracy of three methods, including chip outputs (NMEA results), a conventional FDE method, and the proposed method, through static and kinematic field experiments across various urban densities. Static tests revealed that the proposed method outperformed the conventional method and chip outputs, achieving accuracies ranging from 1.7m to 11.5m, whereas the accuracy of NMEA ranged from 4.2m to 57.4m. Analysis of the cumulative distribution of errors showed that the proposed method yielded the highest percentage of solutions falling within a smaller error range, achieving superior accuracy ranging from 1.8m to 8.5m across urban densities. Additionally, the proposed method demonstrated a remarkable improvement rate of approximately 77% over chip outputs in all urban settings. While the conventional method exhibited improved accuracy in low- and middle-density urban settings, its availability decreased in denser areas. In contrast, the proposed method maintained high accuracy and availability rates across all urban settings.

The kinematic test, conducted in Hong Kong, comprising varying urban settings, further validated the method. Chip outputs exhibited an average accuracy of 27.6 meters, with errors reaching up to 90 meters in highly dense urban areas. The proposed method reduced maximum errors to 40m and improved the overall RMS to 12.9m, indicating a 52.4% enhancement with a full availability rate of 100% with the EKF method. Additionally, our method improved the proportion of moderate-accuracy(<10m) and reduced large errors (>20 m), demonstrating superior consistency in challenging environments. These results illustrate the effectiveness of the proposed method in enhancing accuracy and reliability under kinematic conditions in deep urban canyons.

It is worth emphasizing that the static and kinematic experiments were conducted at different times and different sites with diverse street orientations and building densities, capturing variability in satellite geometry, constellation availability (GPS, BeiDou, etc.), and signal conditions. The consistent accuracy improvements observed across all these varied scenarios—with RMS error reduced from 57.4 m to 8.5 m in the most challenging static test and from 27.6 m to 12.9 m in the kinematic test—demonstrate that the proposed method's gains are robust to changes in trajectory, time, and constellation conditions. To quantify the computational overhead of the proposed method, we profiled the GWSC step on the Huawei P40 device used in all experiments. The grid scoring (including PDR trajectory generation, residuals calculation, and residual clustering) requires approximately 18-25 ms per epoch for all grids since we have simplified the calculation procedures in Section II, depending on the number of candidate grids and satellites tracked. The two-stage FDE step adds another 250-350 ms per epoch, where matrix operation for grid movement costs more time, depending on the PDR trajectory and candidate grids. The total processing time is well within the 1 Hz GNSS measurement interval (1000 ms) and leaves time for other processing tasks. Thus, the proposed method achieves substantial accuracy improvements with an acceptable increase in computational load, making it highly suitable for real-time implementation on consumer-grade devices.

Building on the findings of this study, several promising directions for future research emerge. First, the proposed method could be extended to vehicle-based navigation by replacing PDR with odometry or inertial navigation systems (INS), leveraging wheel speed sensors and steering angle data. Second, incorporating machine learning techniques—such as lightweight neural networks for real-time LOS/NLOS classification—could further refine the fault detection stage. Third, the current grid-based approach could be optimized using adaptive grid resolution or particle filtering to reduce

computational overhead in large-scale deployments. Finally, deploying and validating the method across a broader range of consumer devices (different brands, IMU qualities, and GNSS chipsets) would provide valuable insights into its generalizability and robustness.

VI. Reference

[1] A. Küpper, *Location-based services: fundamentals and operation*. New York: John Wiley & Sons, 2005.

[2] C. R. Drane and C. Rizos, *Positioning systems in intelligent transportation systems*. London: Artech House, Inc., 1998.

[3] A. F. G. G. Ferreira, D. M. A. Fernandes, A. P. Catarino, and J. L. Monteiro, "Localization and positioning systems for emergency responders: A survey," *IEEE Communications Surveys & Tutorials,* vol. 19, no. 4, pp. 2836-2870, 2017.

[4] J. Liu, R. Chen, L. Pei, R. Guinness, and H. Kuusniemi, "A hybrid smartphone indoor positioning solution for mobile LBS," *Sensors,* vol. 12, no. 12, pp. 17208-17233, 2012.

[5] F. Zangenehnejad and Y. Gao, "GNSS smartphones positioning: Advances, challenges, opportunities, and future perspectives," *Satellite navigation,* vol. 2, pp. 1-23, 2021.

[6] M. Petovello, "What are the actual performances of GNSS positioning using smartphone technology?," *InsideGNSS,* vol. 9, pp. 34-37, 2014.

[7] P. D. Groves and Z. Jiang, "Height aiding, C/N 0 weighting and consistency checking for GNSS NLOS and multipath mitigation in urban areas," *The Journal of Navigation,* vol. 66, no. 5, pp. 653-669, 2013.

[8] L. Wang, P. Groves, and M. Ziebart, "GNSS Shadow Matching: Improving Urban Positioning Accuracy Using a 3D City Model with Optimized Visibility Prediction Scoring," in *ION GNSS 2012*, Nashville, Tennessee, 2012.

[9] D. Weng, W. Chen, S. Ji, and J. Wang, "Intelligent urban positioning using smartphone-based GNSS and pedestrian network," *IEEE Internet of Things Journal,* vol. 11, no. 12, pp. 22537-22549, 2024.

[10] J. M. Tranquilla, J. Carr, and H. M. Al-Rizzo, "Analysis of a choke ring groundplane for multipath control in global positioning system (GPS) applications," *IEEE Transactions on antennas and propagation,* vol. 42, no. 7, pp. 905-911, 1994.

[11] L. Garin and J.-M. Rousseau, "Enhanced strobe correlator multipath rejection for code & carrier," in *Proceedings of the 10th International Technical Meeting of the Satellite Division of The Institute of Navigation (ION GPS 1997)*, Kansas City, USA, 1997, pp. 559-568.

[12] M. H. Keshvadi, A. Broumandan, and G. Lachapelle, "Analysis of GNSS beamforming and angle of arrival estimation in multipath environments," in *Proceedings of the 2011 International Technical Meeting of The Institute of Navigation*, 2011, vol. 1, pp. 427-435.

[13] Z. Jiang and P. D. Groves, "NLOS GPS signal detection using a dual-polarisation antenna," *GPS solutions,* vol. 18, no. 1, pp. 15-26, 2014.

[14] Z. Jiang, P. D. Groves, W. Y. Ochieng, S. Feng, C. D. Milner, and P. G. Mattos, "Multi-constellation GNSS multipath mitigation using consistency checking," in *Proceedings of the 24th International Technical Meeting of The Satellite Division of the Institute of Navigation (ION GNSS 2011)*, Portland, OR, USA, 2011: Institute of Navigation, pp. 3889-3902.

[15] L.-T. Hsu, H. Tokura, N. Kubo, Y. Gu, and S. Kamijo, "Multiple faulty GNSS measurement exclusion based on consistency check in urban canyons," *IEEE Sensors Journal,* vol. 17, no. 6, pp. 1909-1917, 2017.

[16] G. Castaldo, A. Angrisano, S. Gaglione, and S. Troisi, "P-RANSAC: An Integrity Monitoring Approach for GNSS Signal Degraded Scenario," *International Journal of Navigation & Observation,* 2014.

[17] A. Angrisano and S. Gaglione, "Smartphone GNSS performance in an urban scenario with RAIM application," *Sensors,* vol. 22, no. 3, p. 786, 2022.

[18] Y. Wen, W. Dai, W. Yu, and L. Pan, "Mitigation of multiple outliers using consistency checking for GNSS standard point positioning in urban areas," *Advances in Space Research,* vol. 73, no. 3, pp. 1721-1733, 2024.

[19] D. Weng, M. Cai, W. Chen, J. Wang, and S. Ji, "GNSS Fault Detection and Exclusion (FDE) under sidewalk constraints for pedestrian localization in urban canyons," *IEEE Transactions on Intelligent Transportation Systems,* vol. 25, no. 9, pp. 11168-11179, 2024.

[20] P. D. Groves, "Shadow matching: A new GNSS positioning technique for urban canyons," *The journal of Navigation,* vol. 64, no. 3, pp. 417-430, 2011.

[21] L. Wang, P. Groves, and M. Ziebart, "GNSS Shadow Matching: Improving Urban Positioning Accuracy Using a 3D City Model with Optimized Visibility Prediction Scoring," *NAVIGATION: Journal of The Institute of Navigation,* vol. 23(3), pp. 44-56, 2013.

[22] L. Wang, P. D. Groves, and M. K. Ziebart, "Smartphone shadow matching for better cross-street GNSS positioning in urban environments," *The Journal of Navigation,* vol. 68, no. 3, pp. 411-433, 2015.

[23] L. Wang, "Kinematic GNSS shadow matching using a particle filter," in *Proceedings of the 27th International Technical Meeting of the Satellite Division of The Institute of Navigation (ION GNSS+ 2014)*, 2014, pp. 1907-1919.

[24] H. Xu, A. Angrisano, S. Gaglione, and L.-T. Hsu, "Machine learning based LOS/NLOS classifier and robust estimator for GNSS shadow matching," *Satellite Navigation,* vol. 1, pp. 1-12, 2020.

[25] H. Luo, D. Weng, and W. Chen, "An Improved Shadow Matching Method for Smartphone Positioning," *Geomatics and Information Science of Wuhan University,* vol. 46, no. 12, pp. 1907-1915, 2021.

[26] H.-F. Ng, G. Zhang, and L.-T. Hsu, "Robust GNSS shadow matching for smartphones in urban canyons," *IEEE Sensors Journal,* vol. 21, no. 16, pp. 18307-18317, 2021.

[27] M. Obst, S. Bauer, and G. Wanielik, "Urban multipath detection and mitigation with dynamic 3D maps for

reliable land vehicle localization," in *Proceedings of the 2012 IEEE/ION Position, Location and Navigation Symposium*, Myrtle Beach, SC, USA, 2012: IEEE, pp. 685-691.

[28] A. Bourdeau, M. Sahmoudi, and J. Tourneret, "Tight integration of GNSS and a 3D city model for robust positioning in urban canyons," in *Proceedings of the 25th International Technical Meeting of the Satellite Division of The Institute of Navigation (ION GNSS 2012)*, 2012, pp. 1263-1269.

[29] T. Suzuki and N. Kubo, "Correcting GNSS multipath errors using a 3D surface model and particle filter," in *Proceedings of the 26th International Technical Meeting of The Satellite Division of the Institute of Navigation (ION GNSS+ 2013)*, Nashville, TN, USA, 2013, pp. 1583-1595.

[30] L.-T. Hsu, Y. Gu, and S. Kamijo, "3D building model-based pedestrian positioning method using GPS/GLONASS/QZSS and its reliability calculation," *GPS solutions,* vol. 20, no. 3, pp. 413-428, 2016.

[31] G. Zhang, H.-F. Ng, W. Wen, and L.-T. Hsu, "3D mapping database aided GNSS based collaborative positioning using factor graph optimization," *IEEE Transactions on Intelligent Transportation Systems,* vol. 22, no. 10, pp. 6175-6187, 2020.

[32] H. Luo, X. Mi, Y. Yang, W. Chen, and D. Weng, "Multi-Epoch Grid-Based 3DMA Positioning in Dense Urban Canyons by Optimizing Reflection Modelling," *IEEE Transactions on Instrumentation and Measurement,* vol. 74, pp. 1-13, 2025, doi: 10.1109/TIM.2025.3545163.

[33] P. D. Groves and M. Adjrad, "Performance assessment of 3D-mapping–aided GNSS part 1: Algorithms, user equipment, and review," *NAVIGATION, Journal of the Institute of Navigation,* vol. 66, no. 2, pp. 341-362, 2019.

[34] H. Luo and W. Chen, "A novel GNSS positioning method for urban canyons in measurement domain," in *Proceedings of the 2023 International Technical Meeting of The Institute of Navigation*, Long Beach, California, USA, 2023, pp. 1129-1142.

[35] R. Sun, J. Wang, Q. Cheng, Y. Mao, and W. Y. Ochieng, "A new IMU-aided multiple GNSS fault detection and exclusion algorithm for integrated navigation in urban environments," *GPS Solutions,* vol. 25, pp. 1-17, 2021.

[36] H. Luo *et al.*, "Integration of GNSS and BLE Technology With Inertial Sensors for Real-Time Positioning in Urban Environments," *IEEE Access,* vol. 9, pp. 15744-15763, 2021.

[37] H. Zhao and Z. Yang, "A Novel Fault Detection and Exclusion Method for Applying Low-Cost INS/GNSS Integrated Navigation System in Urban Environments," *IEEE Transactions on Intelligent Transportation Systems,* 2024.

[38] C. Jiang *et al.*, "Implementation and performance analysis of the PDR/GNSS integration on a smartphone," *GPS Solutions,* vol. 26, no. 3, p. 81, 2022.

[39] X. Niu, Z. Liu, L. Ding, and J. Kuang, "A robust GNSS/INS integrated system for pedestrian navigation in urban environments based on spatial consistency check," *IEEE Internet of Things Journal,* 2025.

[40] G. Guo *et al.*, "Large-scale indoor localization solution for pervasive smartphones using corrected acoustic signals and data-driven PDR," *IEEE Internet of Things Journal,* vol. 10, no. 17, pp. 15338-15349, 2023.

[41] S. Guo, Y. Zhang, X. Gui, and L. Han, "An improved PDR/UWB integrated system for indoor navigation applications," *IEEE Sensors Journal,* vol. 20, no. 14, pp. 8046-8061, 2020.

[42] C. Jiang *et al.*, "Smartphone PDR/GNSS integration via factor graph optimization for pedestrian navigation," *IEEE Transactions on Instrumentation and Measurement,* vol. 71, pp. 1-12, 2022.

[43] R. S. Naser, M. C. Lam, F. Qamar, and B. Zaidan, "Smartphone-based indoor localization systems: A systematic literature review," *Electronics,* vol. 12, no. 8, p. 1814, 2023.

[44] J. Wang *et al.*, "Tightly Coupled Bluetooth Enhanced GNSS/PDR System for Pedestrian Navigation in Dense Urban Environments," *IEEE Transactions on Instrumentation and Measurement,* 2024.

[45] S. Feng, W. Y. Ochieng, D. Walsh, and R. Ioannides, "A measurement domain receiver autonomous integrity monitoring algorithm," *GPS Solutions,* vol. 10, pp. 85-96, 2006.

[46] K. Zhang and P. Papadimitratos, "Fast multiple fault detection and exclusion (FM-FDE) algorithm for standalone GNSS receivers," *IEEE Open Journal of the Communications Society,* vol. 2, pp. 217-234, 2021.

[47] A. Wahdan, J. Georgy, W. F. Abdelfatah, and A. Noureldin, "Magnetometer calibration for portable navigation devices in vehicles using a fast and autonomous technique," *IEEE Transactions on Intelligent Transportation Systems,* vol. 15, no. 5, pp. 2347-2352, 2014.

[48] S. G. Bednarz, "Adaptive modeling of GPS receiver clock for integrity monitoring during precision approaches," Master's Thesis, Massachusetts Institute of Technology, 2004.

[49] A. Jain and S. Schön, "Performance evaluation of GNSS receiver clock modelling in urban navigation using geodetic and high-sensitivity receivers," *The Journal of Navigation,* vol. 74, no. 6, pp. 1397-1415, 2021.

[50] S. Hilla and M. Cline, "Evaluating pseudorange multipath effects at stations in the National CORS Network," *GPS Solutions,* vol. 7, pp. 253-267, 2004.

[51] M. Ester, H.-P. Kriegel, J. Sander, and X. Xu, "A density-based algorithm for discovering clusters in large spatial databases with noise," in *Kdd*, 1996, vol. 96, no. 34, pp. 226-231.

[52] D. Weng, W. Chen, M. Ding, and S. Liu, "Sidewalk matching: a smartphone-based GNSS positioning technique for pedestrians in urban canyons," *Satellite Navigation*, 2025

Huan Luo received the B.Sc and M.Sc degrees in Geomatics engineering from the Northeastern University, Shenyang, China, in 2013 and 2015 respectively, and the Ph.D. degree in 2022 from The Hong Kong Polytechnic University, and now she is currently a Postdoctoral Fellow with the Department of Land Surveying and Geo-Informatics, The Hong Kong Polytechnic University. Her research interests include GNSS positioning in challenging environments, multipath mitigation, and multi-sensor integration for pedestrian localization.

Duojie Weng received the B.S. and M.S. degrees in electrical engineering from Hohai University, Nanjing, China, in 2007 and 2010, respectively, and the Ph.D. degree from The Hong Kong Polytechnic University, Hong Kong, in 2016. He is currently an Assistant Professor with Shenzhen University University. His research interests include urban positioning, integrity monitoring of GNSS, kinematic GPS, and sensor integration for various navigation systems.

Ahmed Mansour is a Postdoctoral Fellow at Hong Kong Polytechnic University (PolyU), Department of Land Surveying and Geo-Informatics (LSGI). He received his Ph.D. degree in 2023 from LSGI. In 2017, he was awarded a Hong Kong Ph.D. Fellowship from the Research Grants Council (RGC). He received his BSc. and MSc. degrees in Civil Engineering and Geomatics at Cairo University, Egypt. His research interests include smartphone positioning, indoor positioning, multi-sensor fusion, crowdsourcing, and cooperative positioning.

Xiaolong Mi is an Assistant Professor in the Department of Land Surveying and Geo-Informatics at The Hong Kong Polytechnic University. He holds PhD degrees in GNSS and Space Geodesy from the University of Chinese Academy of Sciences and in Spatial Sciences from Curtin University. His current research focuses on GNSS and Low Earth Orbit (LEO) technologies for positioning, navigation and timing (PNT), lunar and planetary PNT, and the application of artificial intelligence (AI) in Space Geodesy.

Yang Yang is now a Research Assistant Professor in Hong Kong Polytechnic University. He has been actively working on GNSS related research for over 10 years. His research mainly focuses on GNSS reflectometry for remote sensing, GNSS passive Radar, GNSS Synthetic Aperture Radar, GNSS Software-Defined-Radio receiver, Signal of Opportunities, GNSS multipath analysis.

Wu Chen received the Ph.D. degree from Newcastle University, Newcastle upon Tyne, U.K., in 1992. He is currently a Chair Professor of Satellite Navigation with the Department of Land Surveying and Geo-Informatics, The Hong Kong Polytechnic University. He has been actively working on GNSS related research for more than 30 years. His main research interests are the GNSS positioning quality evaluation, system integrity, various GNSS applications, seamless positioning, and SLAM.